

Study on Dynamic Mechanical Properties of Bedding Shale Under Impact Load

Hongmei Cheng

China University of Mining and Technology

Yunhu Feng (✉ TS20030005A31@cumt.edu.cn)

China University of Mining and Technology

Guangming Xiao

China University of Mining and Technology

Xiangqi Zhang

China University of Mining and Technology

Heng Chen

China University of Mining and Technology

Research Article

Keywords: SHPB, Different bedding dip angles, Different loading rates, Fractal dimension

Posted Date: July 19th, 2022

DOI: <https://doi.org/10.21203/rs.3.rs-1841683/v1>

License:  This work is licensed under a Creative Commons Attribution 4.0 International License.

[Read Full License](#)

Study on Dynamic Mechanical Properties of Bedding Shale Under Impact Load

Hongmei Cheng¹², Yunhu Feng^{*12}, Guangming Xiao^{*12}, Xiangqi Zhang¹², Heng Chen¹²

1. State Key Laboratory for Geomechanics and Deep Underground Engineering; China University of Mining and Technology, Xuzhou, Jiangsu 221008, China

2. School of Mechanics and Civil Engineering; China University of Mining and Technology; Jiangsu, 221116, China

Abstract

In the actual mining process of shale gas, the loads and disturbances imposed on shale by man-made activities are a dynamic process. Therefore, the study of the dynamic constitutive theory of bedding shale under impact load has important theoretical value for the study of fracturing reformation of shale reservoirs and shale gas production. The objective is to explore the dynamic mechanical properties and fracture characteristics of shale with different bedding dip angles under medium and high strain rate loading. The split Hopkinson bar (SHPB) is used to conduct rock dynamic tests on shales with bedding dip angle of 0°, 30°, 60°, 90°. Based on fractal theory, we calculate the relationship between fractal dimension and broken fragments. The results show that the compressive strength and elastic modulus of shale change slowly when loaded at low strain rate, but when loaded at high strain rate, its compressive strength and elastic modulus increase significantly. The failure mode of shale is also transitioned from splitting failure at low strain rate to shear failure at high strain rate. Under high strain rate loading, the impact of loading rate on the dynamic mechanical properties of shale is greater than that of bedding dip. The mechanical behavior of shale under dynamic load is of great significance to the safe exploitation of shale gas and other resources.

Keywords: SHPB; Different bedding dip angles; Different loading rates; Fractal

* Corresponding author.

E-mail address: hmcheng@cumt.edu.cn

dimension

Introduction

In the actual mining process of shale gas, the loads and disturbances imposed on shale by man-made activities such as drilling, perforation, and fracturing are not strictly quasi-static, but a dynamic process. Therefore, the study of the dynamic constitutive theory of bedding shale under impact load has important theoretical value for the study of fracturing reformation of shale reservoirs and shale gas production. In this paper, the SHPB device is used to carry out impact tests on shale with different bedding dip angles to study its dynamic mechanical properties.

In 1914, Hopkinson[1] designed and produced the Hopkinson pressure bar for the first time, which can record the relationship between impact pressure and time. In 1948, Davies[2] designed the use of capacitive sensors to measure axial stress and axial strain in impact experiments. In 1949, Kolsky[3] designed a separate Hopkinson pressure bar for the first time based on Davies' stress-strain test plan. In 1963, Lindholm[4] used strain gauges instead of capacitive sensors to measure the signals of separate bars for the first time. In 1968, Kumar[5] used SHPB for the first rock dynamics test. Since then, SHPB device has become a classic test device for studying the dynamic properties of materials under impact load. Because the strain rate range ($10^2\sim 10^4\text{s}^{-1}$) involved in the Hopkinson bar experimental technology is the range where the sensitivity of the rock response to strain rate changes drastically in rock blasting, roadway excavation, coal falling, etc., therefore, the split Hopkinson bar experimental technology has been widely used.

Based on the SHPB device, domestic and foreign scholars have conducted dynamic tests on a variety of rock materials. Rinehart et al. verified in 1965 that the peak strength of rock under impact load increases with the increase of strain rate. Gomez et al[6]. conducted a series of dynamic and static tensile splitting tests on concrete and granite specimens in 2001 to study the effect of damage on their tensile strength. Friedman[7] conducted impact tests on granite and limestone with loading strain rates of $10^{-1}\sim 10^{-3}/\text{s}$ in 1970. Tanusree Chakraborty[8] studied the dynamic mechanical characteristics of dolomite, limestone and quartzite in 2016. It can be seen

that the current researches on the dynamic mechanical properties of rocks under impact load are mostly concentrated on granite, marble, sandstone and other rocks[9-13], and there are relatively few studies on the dynamic characteristics of bedding shale. Therefore, this paper uses the SHPB device to carry out impact tests on shale with different bedding dip angles, and conducts research on its dynamic mechanical behavior. The research results can provide certain data support for the safe and efficient mining of shale gas.

Split Hopkinson bar test device and principle

The device used in the experiment is a $\Phi 50\text{mm}$ split Hopkinson bar manufactured by Luoyang Liwei Technology Co., Ltd. The schematic diagram of the device, as shown in Fig. 1. It mainly includes a high-pressure gas cylinder, a launch cavity, a cylindrical striker, an incident bar, a transmission bar, an absorbing bar and a buffer device. The data acquisition device is LK2107 super dynamic strain gauge. After the super dynamic strain gauge is connected with the strain gauge, the waveform signal in the bar can be collected. The super dynamic strain gauge used in the experiment has a sensitivity of $0.001\text{V}/\mu\epsilon$, a bridge pressure of 2V , and a gain multiplier is 1000 , and the bridge connection mode is an opposite-arm half bridge.

The principle of the SHPB test is based on two assumptions, and the results are valid only when the sample data is analyzed on the basis of satisfying the two assumptions. The two specific assumptions are as follows:

1) One-dimensional stress wave assumption. In the whole test process, the propagation direction of the stress wave in the bar is one-dimensional, and no dispersion effect occurs. The diameter of the test bar is 50mm , which is much smaller than its length of 3m . The influence of the dispersion effect is very small and can be ignored. Therefore, it can be considered that the one-dimensional stress wave assumption is satisfactory.

2) Assumption of stress equilibrium [14]. The condition to satisfy the assumption of stress equilibrium on the two end faces of the specimen. In fact, due to the propagation of stress waves in the specimen, the stresses at both ends of the specimen

are always unequal. Refer to the "Hopkinson Bar Experiment Technology" written by Fangyun Lu et al. It is believed that when the stress difference between the two ends of the sample is less than 5%, the stress balance can be considered

Taking the Δx micro-segment in the experimental bar, assuming that the bar only undergoes elastic deformation during the loading process, and the cross-section is still flat. Then it can be derived from Newton's second law as follows:

$$\frac{\partial \sigma}{\partial x} A \Delta x = \rho A \Delta x \frac{\partial^2 u}{\partial t^2} \quad (1)$$

Where A is the area of the bar, and ρ is the density of the bar. Combining $v = \frac{\partial u}{\partial t}$,

$\varepsilon = \frac{\partial u}{\partial x}$, $\sigma = E\varepsilon$, the equation can be written as follows:

$$\rho \frac{\partial^2 u}{\partial t^2} = E \frac{\partial^2 u}{\partial X^2} \quad (2)$$

Substituting $c_0 = \sqrt{\frac{E}{\rho}}$ into the above formula, a typical one-dimensional wave equation can be obtained as follows:

$$\frac{\partial^2 u}{\partial t^2} = c_0^2 \frac{\partial^2 u}{\partial x^2} \quad (3)$$

A general solution of the equation (3) can be given as follows:

$$u(X, t) = F_1(X + c_0 t) + F_2(X - c_0 t) \quad (4)$$

Where F_1 and F_2 are the left traveling wave function and the right traveling wave function respectively. For the linear elastic wave, the left-traveling wave and the right-traveling wave satisfy the principle of linear superposition. They can be considered to be independent of each other. Therefore, it can be simplified to just consider initially the right traveling wave in the elastic bar in the static and free state, the above formula(4) can be simplified as follows:

$$u(X, t) = F(X - c_0 t) \quad (5)$$

Taking the derivative of formula (5) with respect to X , the following formulas can

be obtained

$$\frac{\partial u}{\partial X} = F'(X - c_0 t) = \varepsilon \quad (6)$$

Taking the derivative of formula (5) with respect to t , we can get

$$\frac{\partial u}{\partial t} = -c_0 F'(X - c_0 t) = v \quad (7)$$

According to formula (3), the following formula can be obtained:

$$v = -c_0 \varepsilon \quad (8)$$

Assuming that the end face of the sample connected with the incident bar is 1, the end face of the sample connected with the transmission bar is 2, and the displacements on the interface 1, 2 during the test are U_1 and U_2 . According to the linear superposition principle of linear elastic waves, the following formulas can be obtained

$$U_1 = c_0 \int_0^t \varepsilon_i - \varepsilon_r d\tau \quad (9)$$

$$U_2 = c_0 \int_0^t \varepsilon_t d\tau \quad (10)$$

$$\varepsilon = \frac{U_1 - U_2}{l_0} = \frac{c_0}{l_0} \int_0^t \varepsilon_i - \varepsilon_r - \varepsilon_t d\tau \quad (11)$$

Taking the derivative of formula (11) with respect to t , the strain rate can be obtained as follows:

$$\dot{\varepsilon} = \frac{c_0}{l_0} (\varepsilon_i - \varepsilon_r - \varepsilon_t) \quad (12)$$

The forces on both ends of the sample are:

$$F_i + F_r = EA(\varepsilon_i + \varepsilon_r) \quad (13)$$

$$F_t = EA\varepsilon_t \quad (14)$$

The average stress in the sample is:

$$\sigma = \frac{EA(\varepsilon_i + \varepsilon_r + \varepsilon_t)}{2A_0} \quad (15)$$

When the stress balance is satisfied, the above formula can be simplified to:

$$\varepsilon = -\frac{2c_0}{l_0} \int_0^t \varepsilon_r d\tau \quad (16)$$

$$\varepsilon_r = -\frac{2c_0}{l_0} \varepsilon_t \quad (17)$$

$$\sigma = \frac{EA}{A_0} \varepsilon_t \quad (18)$$

That is to say, under the condition of satisfying the stress balance, the formula for calculating the mechanical variables using the two-wave method is (16)- (18).

Test plan and result analysis

Test plan

The sample selected for this test is a cylindrical shale with a height of 25mm, a diameter of 50mm, and a length-to-diameter ratio of 0.5. Table 1 lists the physical parameters of the rock sample. During the test, the specimen is clamped between the incident bar and the transmission bar. Vacuum silicone grease is applied between the alloy bar and the contact surface of the specimen to ensure that the stress wave propagates well between the interfaces. The bullet punch is driven by the high pressure nitrogen to hit the incident bar. A stress pulse σ_I is generated in the incident bar. The incident wave propagates in the incident bar at wave speed $c_0 = \sqrt{E/\rho}$. When reaching the sample, part of the incident wave is reflected back to the incident bar in the form of reflected wave σ_R . A part of it passes through the sample and is transmitted to the transmission bar in the form of transmitted wave σ_T . The incident strain ε_I and the reflected strain ε_R can be measured by the strain gauge attached to the incident bar, and the transmission Strain ε_T is measured by the strain gauge attached to the transmission bar. The bonding method of the strain gages is to paste on the same circle on each bar 180° apart. The stress wave captured by the strain gauge is converted into an electrical signal for storage, and analyzed after the end of the test.

Analysis of test results

Verification of stress balance

In the SHPB experiment, ensuring the axial stress balance can improve the authenticity and validity of the experimental results. According to the experimental principle of SHPB, the equation (19) can be used to verify the stress balance problem

of shale SHPB test.

$$\varepsilon_i + \varepsilon_r = \varepsilon_t \quad (19)$$

In order to achieve stress balance as soon as possible, a rubber sheet with a diameter of 12mm is used as the shaper material, and its plastic waveform is used to shape the incident wave, effectively smoothing the loading front of the wave, and turning the rectangular wave into a sine wave. Taking the shale with 0° bedding dip as an example, the Stress balance diagram and waveform diagram, as shown in Fig. 2.

It can be seen from Fig. 2 that the curve of the incident wave plus the reflected wave and the transmitted wave curve overlap well, basically satisfying that the stress difference between the two ends of the sample is less than 5%. It can be considered that the stress balance is reached. In this test, in order to reach the stress balance as soon as possible, a rubber sheet with a diameter of 12 mm was used as a shaper to shape the incident wave. It can be seen from the waveform diagram and the stress balance diagram that after the use of a shaper, the incident wave becomes a sine wave, the waveform is smoother, and the falling time of the incident waveform becomes longer, which makes it easy to achieve stress balance.

Analysis of dynamic mechanical characteristics of jointed shale under impact load

In this test, SHPB tests with impact pressures of 0.2MPa, 0.3MPa, 0.4MPa, 0.5MPa and 0.6MPa were carried out on shale samples with bedding angles of 0°, 30°, 60°, and 90°. Fig. 3 shows the dynamic stress-strain curves of the four bedding dip shale under different impact pressures. And their dynamic mechanical characteristic parameters, as shown in Table 2.

It can be seen from Fig. 3 that under impact load, the stress-strain curve of shale roughly presents four stages: compaction stage—elastic deformation stage—crack unsteady growth stage—unloading stage.

- 1) **Compaction stage:** The stress-strain curve in this stage shows a Downward concave trend. There are two reasons for this stage. One is that the original sample of shale has not only bedding and joints, but also a large number of micro-cracks and pores. The presence of vacuum silicone grease at both ends

-
- of the sample and the bar causes the two to not be in complete close contact. During the test, there will also be an extremely short compaction transition period caused by the bar first contacting the surface of the coupling agent.
- 2) Elastic deformation stage: At this stage, the slope of the curve rises approximately in a straight line. Under the action of external load, there is almost no crack propagation and the generation of new cracks. Only the original cracks in the sample are in a stable state or a small amplitude change. There is no qualitative change in the elastic deformation state of the rock.
 - 3) Unsteady crack growth stage: In this stage, the stress growth rate slows down and gradually stagnates, and the original cracks expand rapidly, accompanied by a large number of new cracks, and finally penetrate the main crack. The maximum stress at this stage corresponds to the compressive strength of the shale under impact load, and the strain at the peak stress is the peak strain.
 - 4) Unloading stage: The stress of the rock decreases rapidly from near the peak value, the ultimate strain increases rapidly, the rock undergoes large deformation, and the bearing capacity decreases rapidly, which is not enough to resist external load and damage. Due to the large deformation of the rock at this stage, the contact form between the rock and the bar is more complicated. Therefore, different stress-strain curves have a large gap after the peak, and they are not the main object of the analysis of mechanical characteristics[15].

Peak strength refers to the stress value corresponding to the highest point on the stress-strain curve of rock material, which is an important rock dynamic mechanical parameter. Fig. 3 shows the curve of the peak strength of the shale sample with four bedding dip angles as a function of the loading strain rate under impact load.

It can be seen from Fig. 4 that the dynamic compressive strength of shale increases with the increase of the loading strain rate, showing a significant strain rate effect. Among them, when the shale with 0° and 90° bedding dips is in the strain rate range of $60\text{s}^{-1}\sim 90\text{s}^{-1}$, the compressive strength does not change significantly. When the strain rate is greater than 90s^{-1} , the compressive strength varies greatly. The compressive

strength of shale with a bedding dip of 30° increases evenly with the change of the loading strain rate. For the shale with a bedding dip of 60°, the compressive strength does not change significantly when the strain rate is less than 115.08s⁻¹. When the strain rate is greater than 100s⁻¹, the compressive strength has improved significantly. It can also be seen from the figure that the overall compressive strength of shale with a bedding dip of 30° is significantly lower than that of shale with other dips. This may be due to the influence of the shale's own bedding dip.

In this paper, the elastic modulus can be calculated by the formula as follows:

$$E = \frac{\sigma_2 - \sigma_1}{\varepsilon_2 - \varepsilon_1} \quad (20)$$

Where σ_1 and σ_2 refer to the stress at 40% and 60% of the peak stress respectively. ε_1 and ε_2 refer to the strain at 40% and 60% of the peak stress respectively.

Fig. 5 shows that the dynamic elastic modulus of shale has a more obvious strain rate effect, which shows a trend of increasing as the loading strain rate increases, and it has a better capacity in the resistance to deformation. Among them, the elastic modulus of shale with a bedding dip of 0° increases slowly with the increase of the loading strain rate when the loading strain rate is lower than 91.32s⁻¹. When the strain rate is higher than 91.32s⁻¹, the elastic modulus significantly increases with increasing strain rate. The dynamic elastic modulus of shale with a bedding dip of 30° is relatively stable with the change of strain rate, and basically increases in a linear manner. When the strain rate of shale with a bedding dip of 60° is lower than 97.93s⁻¹, the change is small. When the strain rate increases from 97.93s⁻¹ to 134.18s⁻¹, the modulus of elasticity increases from 8.70GPa to 27.78GPa, which is a larger increase. When the strain rate of 90° shale is lower than 81.10s⁻¹, the increase is small. When the strain rate is higher than 81.10s⁻¹, there is a significant increase. And the elastic modulus of 30° bedding dip angle shale is lower than others.

Failure mode analysis of shale impact test

After the impact loading test, the failure modes of shale with different bedding dip angles at different strain rates, as shown in Fig. 6.

It can be seen from Fig. 6 that with the larger the impact pressure loaded, The smaller the fragmentation of the shale sample, the greater the number of fragments, and the more severe the damage. At low strain rates, the failure mode is dominated by splitting failure along the diameter direction. As the loading strain rate increases, shear failure occurs. Among them, the shale with a bedding dip of 0° is a split failure along the diameter when the strain rate is 55.74s^{-1} , which is mainly broken into two relatively complete pieces with less debris, and the strain rate reaches 91.13s^{-1} , the number of damaged blocks increases, but it can be seen that the failure mode is still mainly along the diameter direction. When the strain rate is greater than 101.32s^{-1} , the number of damaged blocks of the sample is more, and the block size is smaller. Which is in the form of shear failure. When the strain rate of the shale with a bedding dip of 60° reaches 115.08s^{-1} , and the strain rate of the shale with a 90° bedding dip reaches 108.34s^{-1} , the damage is more serious. The shale with a bedding dip of 30° is seriously damaged when the strain rate is greater than 99.05s^{-1} . It can be seen that the shale with a bedding dip of 30° has the lowest bearing capacity under impact load. On the whole, as the loading strain rate increases, shale gradually transitions from a mode dominated by splitting failure to a mode dominated by shear failure.

Taken together, as the strain rate increases, the number of micro-cracks in the process of shale failure increases significantly, and the expansion of micro-cracks consumes more energy. Due to the short time in the SHPB test, there is not enough time to complete the sample energy accumulation. Therefore, the stress in the specimen will increase to balance the external energy, and therefore, the strength of the specimen will increase with the increase of the strain rate.

Fractal dimension calculation

Fractal theory was first proposed by Mandelbrot. At the end of the 20th century, rock mechanics scholars introduced fractal theory into rock mechanics to study the nonlinear problems in describing the shape and mechanical properties of complex rock natural structures[16-18].

Use a standard sieve to screen the rock sample after the experiment, the fractal

dimension D can be calculated by the following formula as [19, 20]:

$$\frac{M(x)}{M_T} = \left(\frac{x}{x_m} \right)^{3-D} \quad (21)$$

Where $M(x)$ and M_T respectively represent the cumulative mass under the sieve and the total mass of the rock sample. x , x_m represent the particle size and maximum particle size of the rock sample fragments, and D is the fractal dimension of rock fragmentation number.

By taking the logarithm of both sides of the formula (21), the equation can be written as:

$$\lg \frac{M(x)}{M_T} = (3-D) \lg \left(\frac{x}{x_m} \right) \quad (22)$$

By linearly fitting the relationship between $\frac{M(x)}{M_T}$ and $\frac{x}{x_m}$ in double logarithmic coordinates, the fractal dimension D can be obtained. Fig. 7 shows the variation curve of $\lg \frac{M(x)}{M_T}$ with $\lg \left(\frac{x}{x_m} \right)$, Fig. 8 shows the variation curve of the fractal dimension with the loading strain rate, and Table 3 shows the fractal dimension D of the rock sample after different impact pressure loading failure.

It can be seen from Fig. 7, Fig. 8 and Table 2 that as the impact pressure increases from 0.2 MPa to 0.6 MPa, the fractal dimension of the 0° bedding dip angle shale after failure increases from 0.4832 to 1.77, which is the largest increase. The fractal dimension of 30° bedding dip shale increased from 0.7256 to 1.8638, the fractal dimension of 60° bedding dip shale increased from 0.9860 to 2.0524, and the fractal dimension of 90° bedding dip shale increased from 1.315 to 1.947. According to the fitting formula, the slope of shale with 0° bedding dip is 0.0198, which is 1.3855 times higher than the 0.0083 of 90° shale. The shale with 30° and 60° bedding dips is 0.0143 and 0.0159. The gap between the two is small. The fractal dimension can reflect the relationship of the degree of fragmentation, which can be seen that the fragmentation degree of the 0° bedding dip angle shale changes most obviously with the load strain rate, and the fracture degree of the 90° shale is least affected by the load strain rate

change. The degree of fragmentation of shale with bedding dip angles of 30° and 60° is between the two affected by strain rate, and there is little difference between the two.

The curve obtained from Figure 8 can be fitted to the linear equation as follows:

$$D = \begin{cases} 0.0198x - 0.7192 & R^2 = 0.7620 & 0^\circ \\ 0.0143x - 0.1029 & R^2 = 0.8150 & 30^\circ \\ 0.0159x - 0.5106 & R^2 = 0.9175 & 60^\circ \\ 0.0083x + 0.777 & R^2 = 0.7771 & 90^\circ \end{cases}$$

The fragmentation coefficient r is defined to further analyze the fracture degree of the rock sample under different loading strain rates. the smaller the value of r , the higher the degree of failure, the r can be calculated by the following formula:

$$r = \sum_{n=1}^6 M_{sn} d_{vn} \quad (23)$$

Where d_{sn} represents the average size of each group of fragments, replaced by the average of the upper and lower limits of the distribution range, and M_{sn} is the proportion of the mass of each group of fragments to the total mass.

Fig. 9 shows the relationship between the fractal dimension D of shale with different bedding dip angles and the average block size distribution r . It can be seen from Fig. 9 that with the increase of the loading strain rate, the smaller the average blockiness r , the larger the fractal dimension D . The slope of the curve can reflect the sensitivity of the fractal dimension to the distribution of blockiness. The larger the slope, the more sensitive the fractal dimension is to changes in the average blockiness distribution. The fractal dimension of shale with 0° bedding dip is more affected by the average block size distribution, and the fractal dimension of 90° shale is less affected by the average block size distribution.

Conclusion

In this paper, dynamic compression tests of bedding shale with four dip angles of 0°, 30°, 60°, and 90° are carried out, and the influence of different impact pressures and different bedding dip angles on the mechanical properties of shale is analyzed in detail. The main conclusions are as follows:

- 1) The compressive strength and elastic modulus of bedding shale changes

slowly when loaded at low strain rates, but when loaded at high strain rates, its compressive strength and elastic modulus are greatly increased. As the strain rate increases, the number of micro-cracks in the shale failure process increases significantly. The expansion of micro-cracks consumes more energy, and the stress in the specimen will increase to balance the external energy. Therefore, the strength of the specimen increases with the strain rate. Its failure mode also varies with the strain rate. In the process of increasing the strain rate from low to high, it gradually transitions from splitting failure to shear failure.

- 2) Through the analysis of the dynamic mechanical characteristics of bedding shale, it can be seen that the mechanical behavior of shale with different bedding dip angles under the same impact load shows different mechanical behaviors. On the whole, the shale strength and modulus of 0° bedding dip is the lowest. The shale with 0° and 90° bedding dip angles has higher strength and modulus, and its compressive capacity is higher.
- 3) The fractal analysis of the broken shale fragments after dynamic loading shows that with the increase of the impact loading strain rate, the smaller the fragmentation of the rock after fracture, the larger the fractal dimension. The 0° bedding dip angle the degree of shale fracture changes most obviously with the load strain rate. The fracture degree of the 90° bedding dip angle shale is the least affected by the load strain rate. The degree of fracture of the shale with bedding dip angle of 30° and 60° is affected by the loading strain rate between the two, and there is not much difference between the two. When the impact pressure reaches 0.6Mpa, the fragmentation distribution coefficients of shale with different inclination angles are not much different, indicating that the bedding inclination has little effect on the particle size distribution of the crushed shale at this time, and the impact load has great effect on the rock sample's size distribution.

Acknowledgements: This work was supported by the Fundamental Research Funds for the Central Universities (2019XKQYMS41).

Declarations

Conflict of Interest: The authors declare no competing interests.

References

- [1] B. Hopkinson. A Method of Measuring the Pressure Produced in the Detonation of High Explosives or by the Impact of Bullets[J]. Proc. R. Soc. London 1914, 89 (612):411-413.
<https://doi.org/10.1098/rsta.1914.0010>
- [2] R. M. Davies. A Critical Study of the Hopkinson Pressure Bar[J]. Philos. Trans. R. Soc. Lond. Ser. A-Math. Phys. Eng. Sci. 1948, 240 (821).
<https://doi.org/10.1098/rsta.1948.0001>
- [3] H. Kolsky. An Investigation of the Mechanical Properties of Materials at very High Rates of Loading[J]. Proceedings of the Physical Society. Section B 1949, 62 (11).
<https://doi.org/10.1088/0370-1301/62/11/302>
- [4] U. S. Lindholm, L. M. Yeakley, A. Nagy. The dynamic strength and fracture properties of dresser basalt[J]. Int. J. Rock Mech. Min. Sci. 1974, 11 (5):181-191.
[https://doi.org/10.1016/0148-9062\(74\)90885-7](https://doi.org/10.1016/0148-9062(74)90885-7)
- [5] A. Kumar. The Effect of Stress Rate and Temperature on the Strength of Basalt and Granite[J]. Geop 1968, 33 (3).
<https://doi.org/10.1190/1.1439947>
- [6] J. T. Gomez, A. Shukla, A. Sharma. Static and dynamic behavior of concrete and granite in tension with damage[J]. Theor. Appl. Fract. Mech. 2001, 36 (1).
[https://doi.org/10.1016/S0167-8442\(01\)00054-4](https://doi.org/10.1016/S0167-8442(01)00054-4)
- [7] F. M., P. R.D., G. S.J. Observation of brittle-deformation features at the maximum stress of westerly granite and solenhofen limestone[J]. Pergamon 1970, 7 (3).
[https://doi.org/10.1016/0148-9062\(70\)90043-4](https://doi.org/10.1016/0148-9062(70)90043-4)
- [8] T. Chakraborty, S. Mishra, J. Loukus et al. Characterization of three Himalayan rocks using a split Hopkinson pressure bar [J]. Int. J. Rock Mech. Min. Sci. 2016, 85.
<https://doi.org/10.1016/j.ijrmms.2016.03.005>
- [9] G. Fengqiang, J. Hangyu, Z. Zongxian et al. Energy Dissipation and Particle Size Distribution of Granite under Different Incident Energies in SHPB Compression Tests[J]. Shock Vibrat. 2020, 2020.
<https://doi.org/10.1155/2020/8899355>
- [10] D. Basu, N. Lam, S. Mishra et al. Characterization of Sandstone for Application in Blast Analysis of Tunnel[J]. Geotech. Test. J. 2020, 43 (2).
<https://doi.org/10.1520/GTJ20180270>
- [11] S. Liu, J. Xu. Effect of Strain Rate on Macro- and Micro-Structural Failure Characteristics of Marble from Split Hopkinson Pressure Bar Tests[J]. Geotech.

-
- Lett. 2019, 9 (3):1-18.
<https://doi.org/10.1680/jgele.19.00009>
- [12] X. Li, S. Wang, Y. Xu et al. Effect of microwave irradiation on dynamic mode-I fracture parameters of Barre granite[J]. Eng. Fract. Mech. 2020, 224.
<https://doi.org/10.1016/j.engfracmech.2019.106748>
- [13] X. Beijing, D. Ai, Y. Yang et al. Crack Detection and Evolution Law for Rock Mass under SHPB Impact Tests[J]. Shock Vibrat. 2019, 2019.
<https://doi.org/10.1155/2019/3956749>
- [14] R. Guo, H. Ren, L. Zhang et al. Research of an SHPB Device in Two-by-Two Form for Impact Experiments of Concrete-Like Heterogeneous Materials [J]. AcMSS 2021, (prepublish).
<https://doi.org/10.1007/S10338-021-00218-Y>
- [15] P. Pei, P. Zhongcai, T. Zhiyong. Numerical and Theoretical Analysis of the Inertia Effects and Interfacial Friction in SHPB Test Systems [J]. Materials 2020, 13 (21).
<https://doi.org/10.3390/ma13214809>
- [16] Y. Ju, Q. Zhang, J. Zheng et al. Fractal model and Lattice Boltzmann Method for Characterization of Non-Darcy Flow in Rough Fractures[J]. Sci. Rep. 2017, 7 (1).
<https://doi.org/10.1038/srep41380>
- [17] Y. Deng, M. Chen, Y. Jin et al. Theoretical analysis and experimental research on the energy dissipation of rock crushing based on fractal theory[J]. J. Nat. Gas Sci. Eng. 2016, 33.
<https://doi.org/10.1016/j.jngse.2016.05.020>
- [18] C. Ai, J. N. Zhang, G. Y. Liu, "The Rock Mass Damage Fragment Distribution of the Fracture for the Wells with Broken Casing," presented at the Applied Mechanics and Materials, 2010.
<https://doi.org/10.4028/www.scientific.net/AMM.29-32.1494>
- [19] H. Xie, *Fractals in Rock Mechanics*. CRC Press, p. 2020.
- [20] Y. Li, R. Huang. Relationship between joint roughness coefficient and fractal dimension of rock fracture surfaces[J]. Int. J. Rock Mech. Min. Sci. 2015, 75:15-22.
<https://doi.org/10.1016/j.ijrmms.2015.01.007>

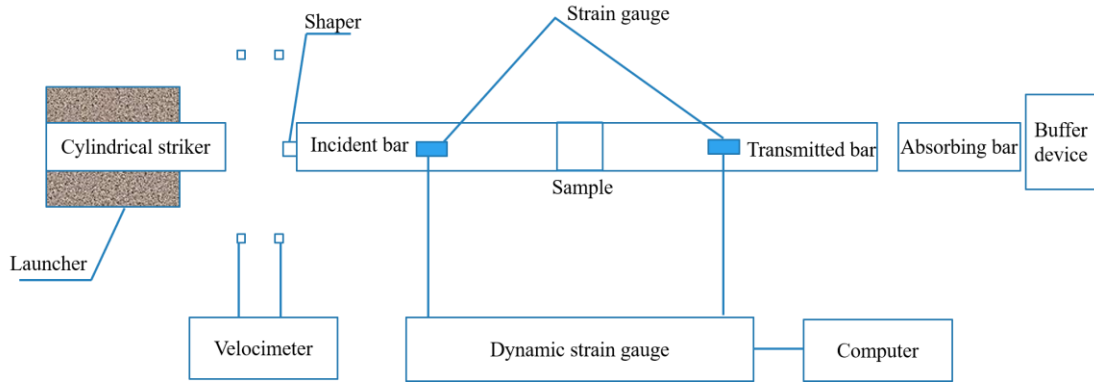


Fig. 1 Split Hopkinson bar simplified diagram

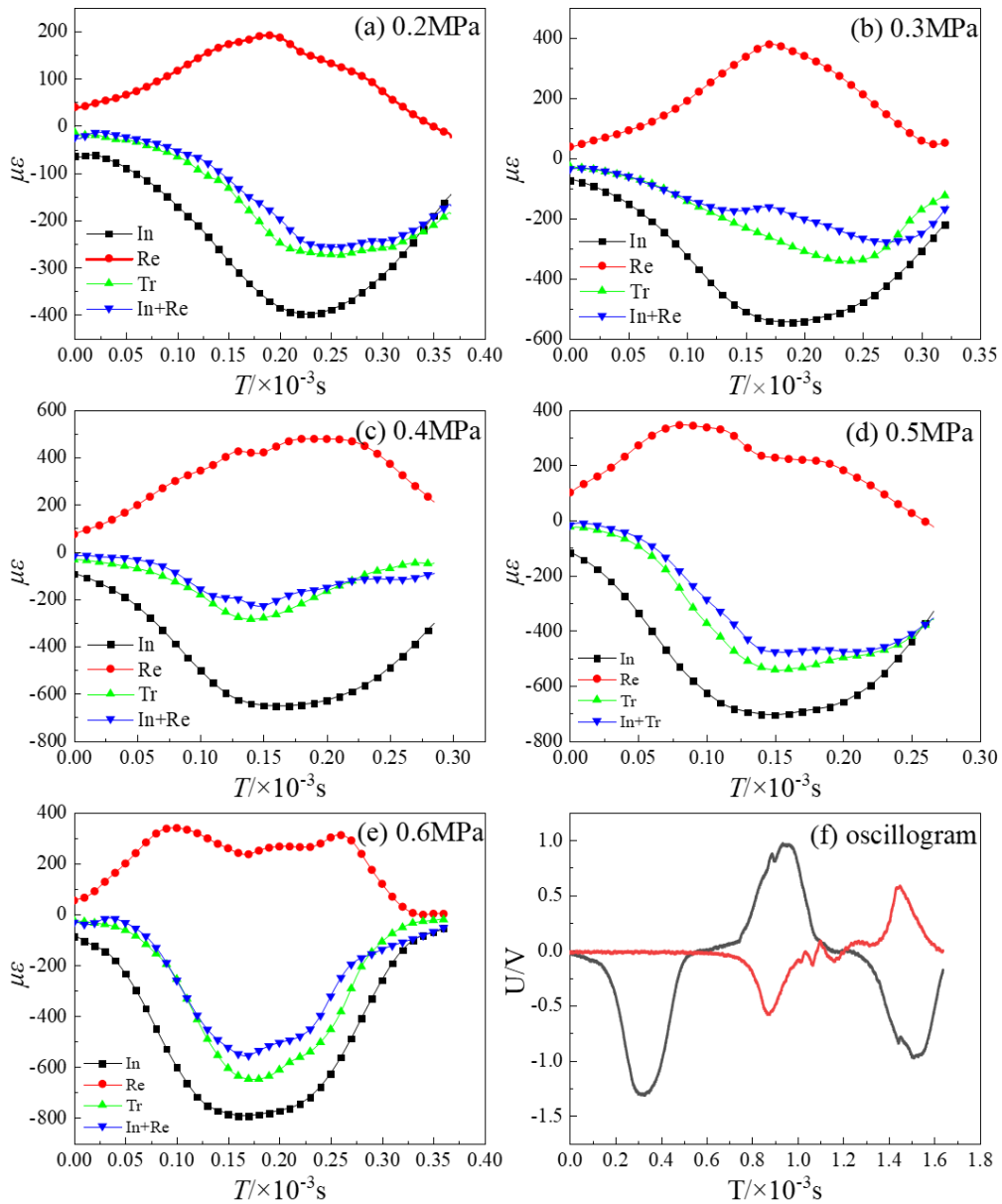


Fig. 2 Stress balance diagram and waveform diagram

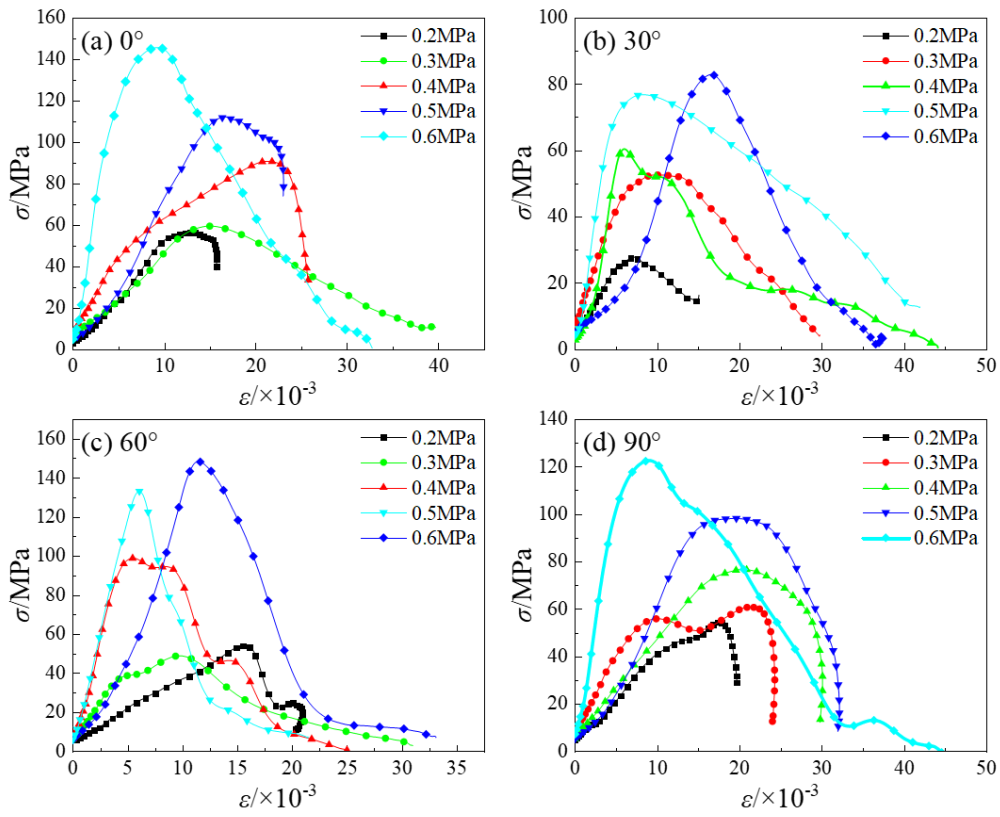


Fig. 3 Stress-strain diagram

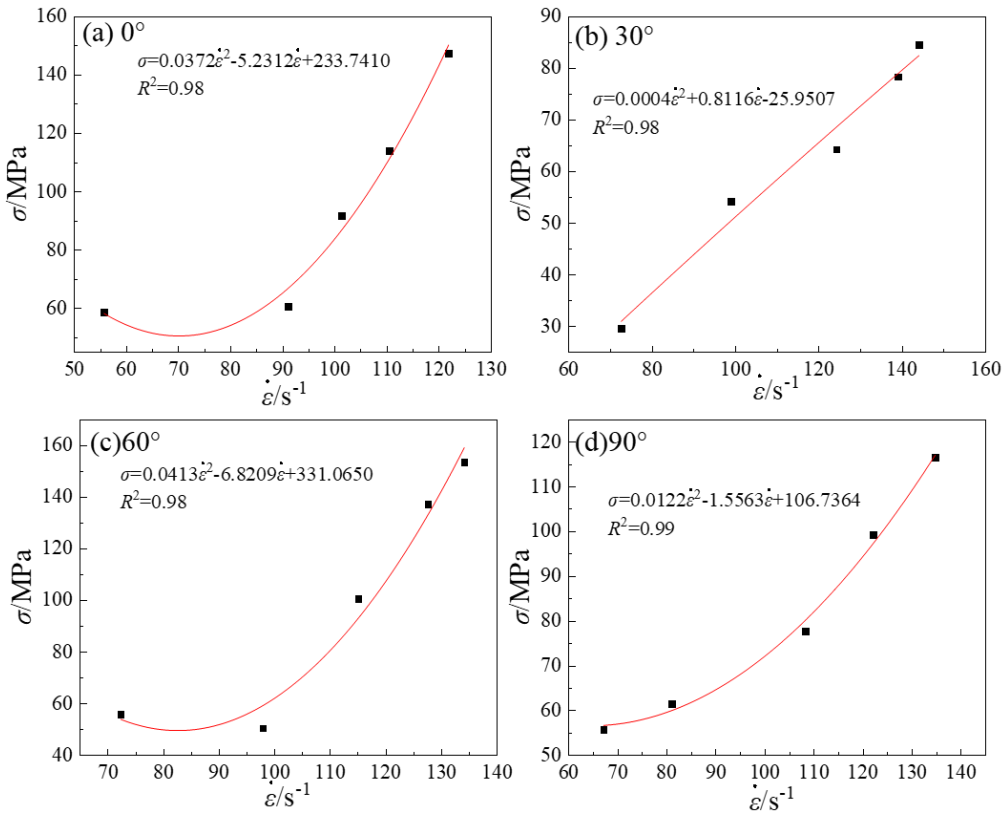


Fig. 4 Variation of strength with strain rate

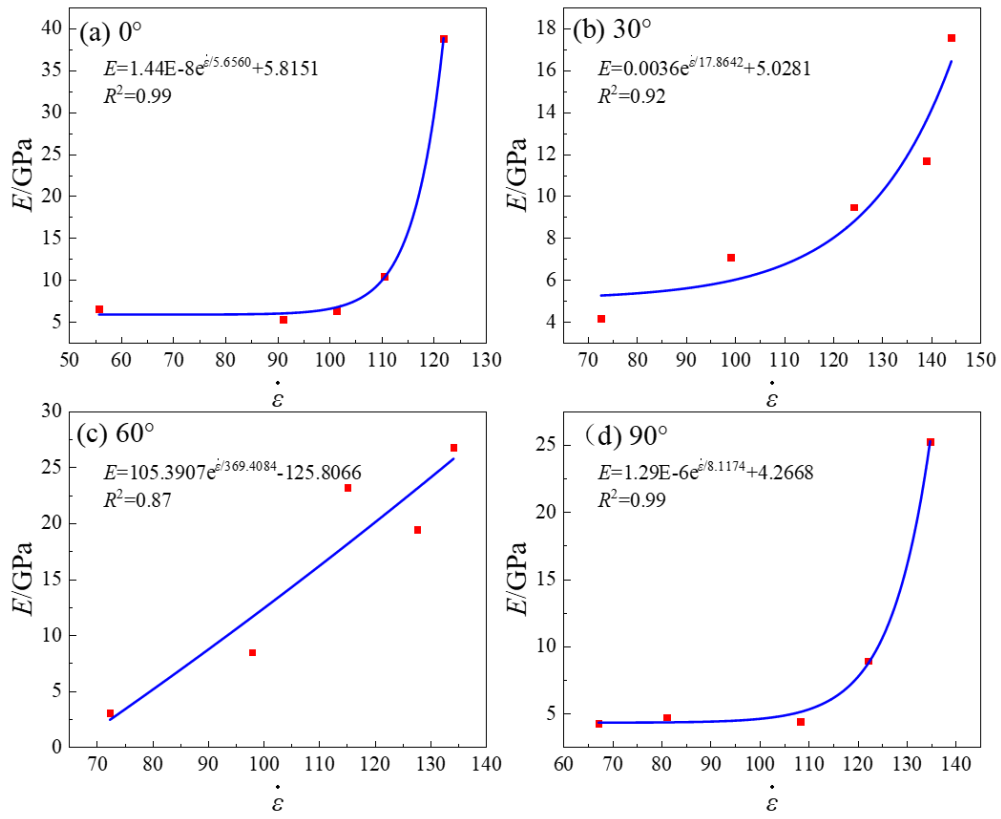


Fig. 5 Variation of elastic modulus with strain rate

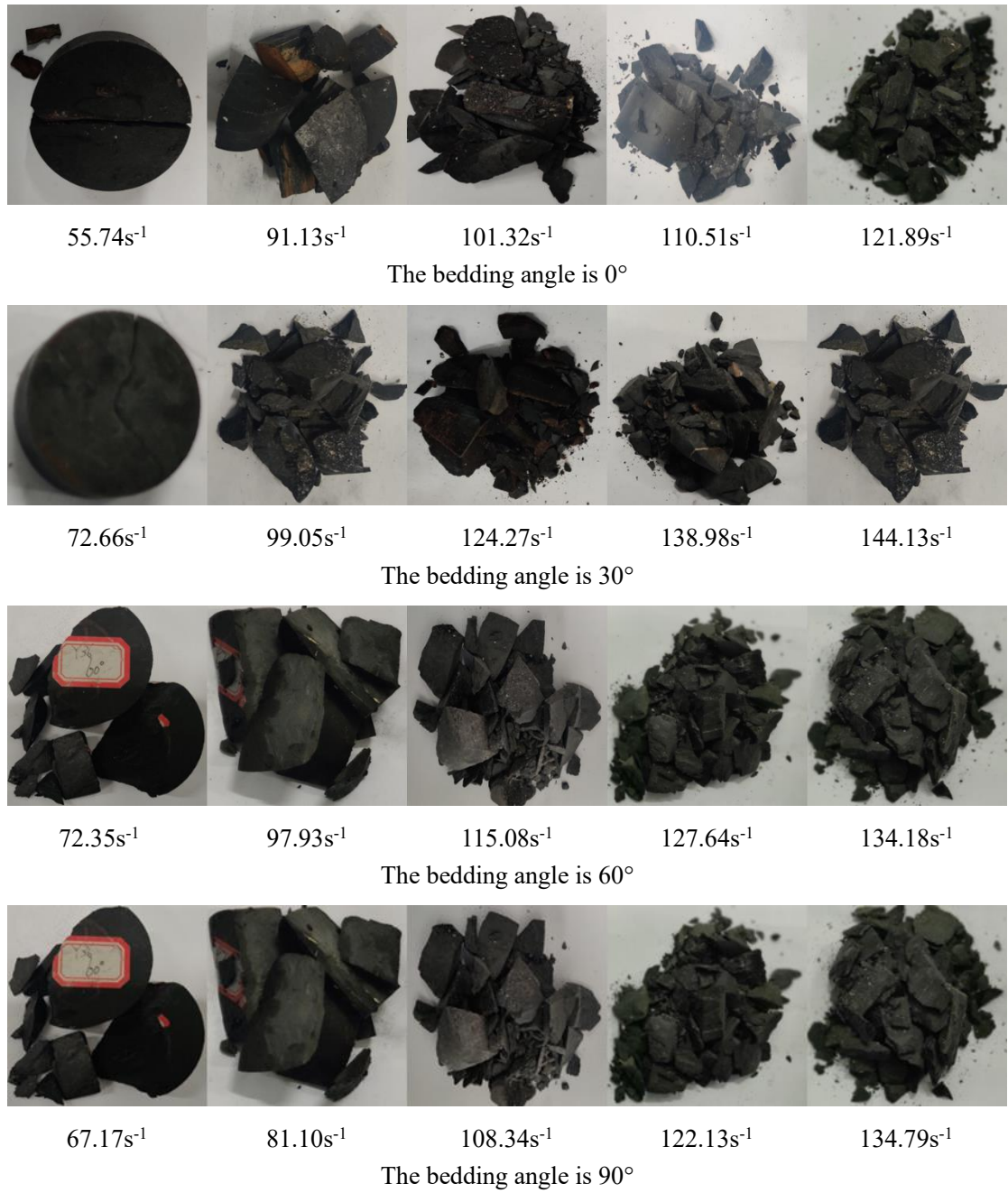


Fig. 6 Dynamic compression failure characteristic diagram of bedding shale

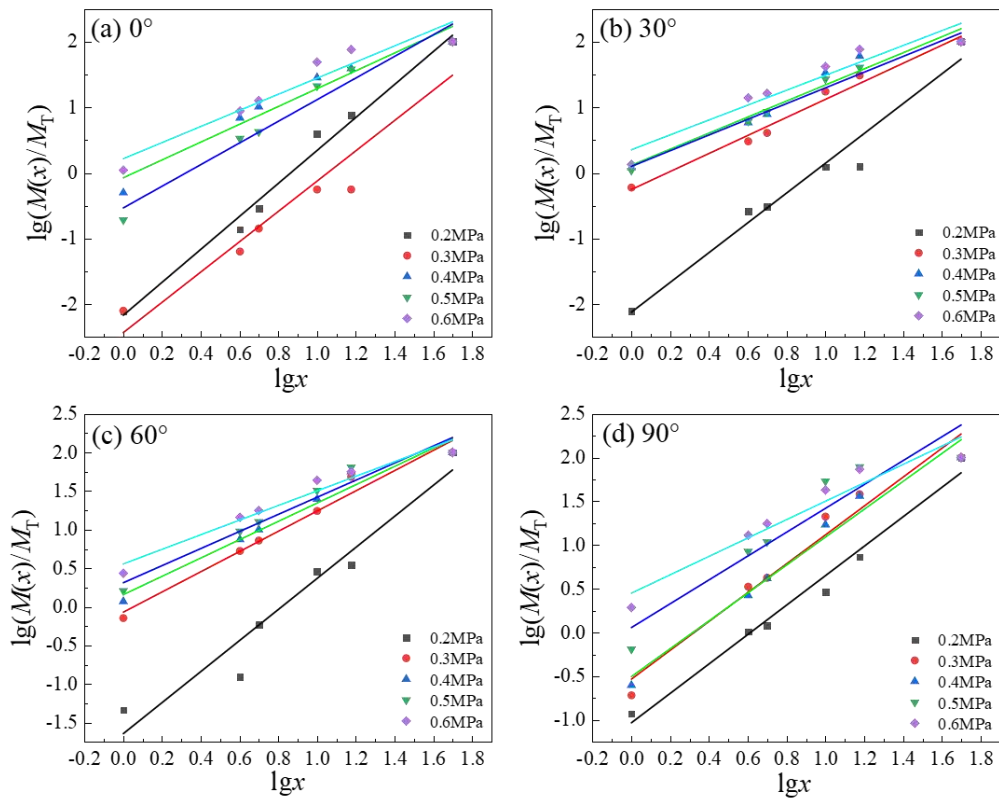


Fig. 7 The relationship between rock mass distribution $\lg \frac{M(x)}{M_T}$ and $\lg \frac{x}{x_m}$

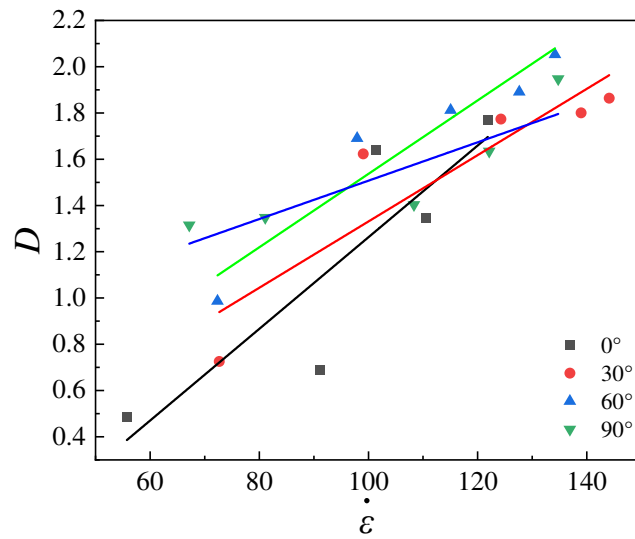


Fig. 8 The relationship between fractal dimension D and strain rate

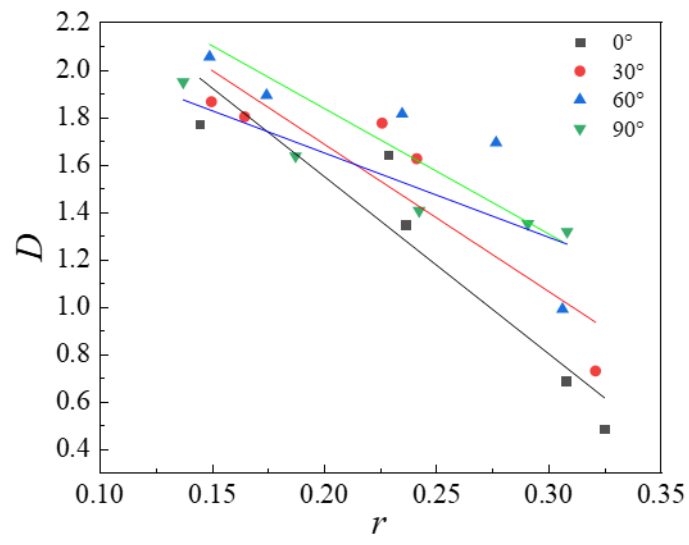


Fig. 9 The relationship between fractal dimension D and blockiness distribution r

Tab.1 Table of physical parameters of dynamic test specimens

Sample No	Bedding dip angle	height mm	diameter mm	Mass g	Density g/cm ³	Wave speed m/s
DY1	0°	50.10	25.03	131.00	2.65	2374
DY2	0°	49.98	25.06	134.10	2.66	2271
DY3	0°	49.83	24.84	127.85	2.64	2342
DY4	0°	50.11	24.85	129.59	2.64	2238
DY5	0°	50.14	25.06	126.46	2.63	2344
DY6	30°	50.14	25.08	134.74	2.66	2437
DY7	30°	49.83	24.73	128.75	2.64	2569
DY8	30°	49.54	24.87	128.77	2.64	2645
DY9	30°	50.07	25.26	136.39	2.67	2658
DY10	30°	49.87	24.93	129.88	2.64	2569
DY11	60°	49.82	25.26	129.58	2.64	2841
DY12	60°	50.12	25.03	134.60	2.66	2910
DY13	60°	50.07	24.99	132.93	2.65	2895
DY14	60°	50.14	25.42	137.20	2.67	2836
DY15	60°	50.15	25.30	132.29	2.65	2746
DY16	90°	50.09	25.05	135.25	2.66	3009
DY17	90°	50.08	24.95	132.81	2.65	3125
DY18	90°	50.27	24.98	135.97	2.66	3129
DY19	90°	50.18	24.87	134.41	2.66	3289
DY20	90°	49.98	24.74	132.88	2.65	3214

Tab.2 Dynamic mechanical characteristic parameters of shale under impact load

Sample No	Bedding dip angle	Impact air pressure(MPa)	Compressive strength(MPa)	Strain rate (s ⁻¹)	Elastic Modulus()
DY1	0°	0.2	58.75	55.74	4.95
DY2	0°	0.3	60.61	91.13	5.41
DY3	0°	0.4	91.64	101.32	5.88
DY4	0°	0.5	113.96	110.51	10.21
DY5	0°	0.6	147.42	121.89	24.84
DY6	30°	0.2	29.64	72.66	4.26
DY7	30°	0.3	54.16	99.05	8.08
DY8	30°	0.4	64.22	124.27	8.79
DY9	30°	0.5	78.31	138.98	14.19
DY10	30°	0.6	84.49	144.13	17.16
DY11	60°	0.2	55.74	72.35	3.11
DY12	60°	0.3	50.49	97.93	8.70
DY13	60°	0.4	100.44	115.08	16.44
DY14	60°	0.5	137.15	127.64	25.70
DY15	60°	0.6	153.34	134.18	27.78
DY16	90°	0.2	55.78	67.17	4.61
DY17	90°	0.3	61.44	81.10	7.21
DY18	90°	0.4	77.65	108.34	6.84
DY19	90°	0.5	99.18	122.13	10.19
DY20	90°	0.6	116.43	134.79	19.29

Tab.3 Fractal dimension calculation table

0°	Impact air pressure (MPa)	0.2	0.3	0.4	0.5	0.6
	Strain rate (s ⁻¹)	55.74	91.13	101.32	110.51	121.89
	Fractal dimension D	0.4832	0.6869	1.6395	1.3476	1.77
	<i>R</i> ²	0.9864	0.9266	0.9484	0.9606	0.9151
30°	Impact air pressure (MPa)	0.2	0.3	0.4	0.5	0.6
	Strain rate (s ⁻¹)	72.66	99.05	124.27	138.98	144.13
	Fractal dimension D	0.7256	1.6229	1.7735	1.8006	1.8638
	<i>R</i> ²	0.9654	0.9827	0.9475	0.9793	0.9135
60°	Impact air pressure (MPa)	0.2	0.3	0.4	0.5	0.6
	Strain rate (s ⁻¹)	72.35	97.93	115.08	127.64	134.18
	Fractal dimension D	0.986	1.69	1.8116	1.891	2.0524
	<i>R</i> ²	0.9421	0.9740	0.9667	0.9558	0.9555
90°	Impact air pressure (MPa)	0.2	0.3	0.4	0.5	0.6
	Strain rate (s ⁻¹)	67.17	81.1	108.34	122.13	134.79
	Fractal dimension D	1.315	1.3476	1.4031	1.6344	1.947
	<i>R</i> ²	0.9819	0.9606	0.9750	0.8920	0.9311